A Time-Average Ocean: Thermal Wind and Flow Spirals

Carl Wunsch,[a]

[a] *Harvard University and MIT*

Cambridge MA

Corresponding author: Carl Wunsch carl.wunsch@gmail.com

ABSTRACT: Using a 26-year average of a dynamically consistent ECCO state-estimate, an effort is made to find descriptive, but nonetheless quantitative patterns of properties of the ocean circulation that are near-globally applicable outside the Arctic regions. Even with a 26-year average, complex spatial variations in the flow field remain, particularly below about 2000m. Nonetheless, certain constructs do describe the great bulk of the ocean. These constructs consist of thermal wind balance (quasi-geostrophy), spiral-like flow behavior in the near-surface boundary layers with orientation analogous to that of an Ekman layer—abruptly changing sign across the equator. In contrast, evidence for beta-spirals is very thin, consistent with the spatially complex meridional and vertical velocities. As expected, integration so as to remove spatial dependence in one coordinate (e.g. zonal) does produce much simplified structures, albeit in the process suppressing diverse dynamical regimes. Predominantly zonal structures persist in the zonal velocity at depth, and are presumed sensitive to the (parameterized) mean eddy fluxes. An unanswered question, and one perhaps unanswerable at the present time, is whether a much longer averaging interval would significantly further simplify the circulation.

KEYWORDS: time-average circulation, state estimate, near-surface flows

1. Introduction

As in a previous paper, Wunsch (2023, hereafter W23) an attempt is made here to extract some simple quantitative principles that are widely applicable when describing the time-averaged global ocean. Present knowledge suggests that the ocean has numerous physically distinct regions, and within those regions each grid point can differ from any others—rendering difficult any sort of generalization. As an example of the challenge, W23 addressed the question of whether the Munk "abyssal recipes"were a generally applicable description of the global ocean below about 1000m? (The answer was "no ".)

Results in both W23 and here are based upon a 26-year uniform time-averaged state estimate (version 4, release 4) from the Estimating the Circulation and Climate of the Ocean (ECCOv4r4; see Wunsch and Heimbach, 2007; Forget et al., 2015; Fukumori et al., 2019) with 1° of horizontal spatial resolution. That estimate has the property, up to numerical accuracy, of obeying all of the physically important time-varying constraints of a system, including conservation laws for energy, mass, vorticity, etc. and the usual no-slip and known flux boundary conditions and so is physically realizable through time. "Obeying" is used in the sense that changes in each of the values of conservation laws can be traced directly to values and changes in forcing and dissipation mechanisms without incurring the errors in these quantities often induced by methods intended to accommodate sequential observations (Wunsch et al., 2023). The estimate also has the important property that it represents a non-linear least-squares fit of a version of the MITgcm to the great majority of global-scale data sets (CTD, Argo, altimetry, scatterometry, meteorological fields, etc. including their uncertainty estimates; see Forget et al., 2015). An alternative statement of the present goal is to ask "what qualitative, but quantifiable, properties of the ocean circulation must be reproduced by any useful near-global description, including those from general circulation models, of its time-average?"

Forget et al. (2015) should be consulted for technical details of the underlying model, data, and the estimation methods. Of particular importance here are the use of the Gaspar et al (1990) near-surface dynamics, the Gent and McWilliams (1990) eddy transport scheme, the Redi (1982) mixing tensor, and other parameterizations of instabilities and mixing. The Appendix has a brief discussion of the role of unresolved boundary layers in the presence of large amounts of interior data.

The present purpose is to further describe a few of the salient phenomena in the global 26-year average, and to determine which properties of the dynamical time-mean solution can, unlike the original abyssal recipes in W23, be used as near-universal descriptors of the near-global ocean. Another example of a hypothetical descriptor would be the statement that in most of the world ocean, the time-mean upper layer velolcities describe an Ekman-like spiral (which proves true). An earlier time-average was described by Forget (2010), but over a considerably shorter time interval (3 years). Numerous pictorial renderings of a 20-year v4r4 average can be seen in http://hdl.handle.net/1721.1/107613, and http://hdl.handle.net/1721.1/109847 or in the Supplemental Material, and with a discussion in Fukumori et al. (2018). Some fields not displayed here, as well as a sketch representation of the time-variability, can be found in those references.

Finding explanatory physics underlying most of the results requires analyses that are found elsewhere. The goal does however, require a minimal sketch of the global circulation and its properties. No claim is made that what follows is a full or definitive description of the time-average oceanic general circulation: a full discussion requires a much longer and elaborate study. Comparisons could be made, for example, with many of the descriptive elements in Talley et al. (2011)—requiring a book. Decisions as to the most useful representations of a three- dimensional global flow are extremely challenging, and to a considerable degree, arbitrary.

An underlying, fundamental,idea, is what might be called the "hypothesis of simplification": that is whether a multi-decade time-average of the circulation is necessarily significantly simpler than a synoptic one. On the one hand, averages tend to simplify by diminishing structures arising from temporally varying phenomena. On the other hand, long-term averages permit the emergence from the masking variability of quasi-steady structures from the the zero-frequency complicated topography and lateral boundaries, and from the influence of inhomogeneities of time-mean forcing and turbulent effects. Which, if any, of these effects will dominate over 26-years and longer is not, a priori, obvious. The simplification hypothesis has a direct bearing e.g., on the utility of a Reynolds decomposition in frequency and/or wavenumber.

Discussion and analysis here are confined to the regions southward of about 60°N—omitting the Arctic regions, which are the subject of a purpose-built state estimation system (Nguyen et al., 2021), one including the important effects of sea ice. Some of the figures do display Arctic structures, but they are not discussed here. Note too, that a higher resolution state estimate of the

Southern Ocean region (Mazloff et al., 2010) and subsequent published analyses of the physics also exist. Much higher resolution global state estimates are available (Menemenlis et al., 2008), but for considerably shorter intervals than being used here. Those are being incrementally extended in time without data constraints apart from the initial conditions—as derived from ECCOv4.[1]

a. Underlying Time Scales

Of the powerful and attractive theories of the ocean circulation (e.g., Sverdrup balance, abyssal recipes, Stommel-Arons flows, etc.) almost all were created in the framework of a laminar steady-state ocean, commonly with simplified topography, and surface and lateral boundary structures. In recent years (e.g., the Wunsch and Ferrari, 2018 review, and numerous other papers), it has become clear that the synoptic ocean is turbulent on many scales and filled with fields of three-dimensional structures, often labelled as "eddies" of a great variety of theoretical and observational types—with no known low frequency cut-off— and including such phenomena as internal waves, too.

Known adjustment times of the large-scale ocean vary from days (some barotropic Rossby wave phenomena), decades (high latitude baroclinic adjustments), and out to many thousands of years (water mass property adjustment times). In that context, 26-years is an extremely short averaging time and the system is surely not in equilibrium. (Gebbie, 2020, discusses the issue of thermal equilibrium in the ocean.) It is nonetheless of interest to understand the extent to which such an average does reduce the complexity of the system, possibly leading to global generalizations. As a rough guide to the structure of temporal stability, Fig. A3 in the Appendix shows the annual standard deviation of current speed at the sea-surface. Many distinct regions already appear. The focus on what follows is on the velocity field—including its connection to in situ density through the quasi-geostrophic thermal wind equations. Central results are mostly pictorial and in the interests of a shorter length, some figures are consigned to an Appendix or to the Supplemental Material.

2. Flow Field

Let u, v, w be the zonal, meridional and vertical velocity components, all understood to be 26-year Eulerian time-average values. The descriptions that follow could be done for Lagrangian or residual mean velocities, but the Eulerian picture is the most straightforward. Local cartesian coordinates

[1]For recent developments in the higher resolution representation and for biological applications, see Carroll et al. (2022) and for a discussion of the role of resolved eddies on Lagrangian flows, see Wang et al. (2022), among other applications.

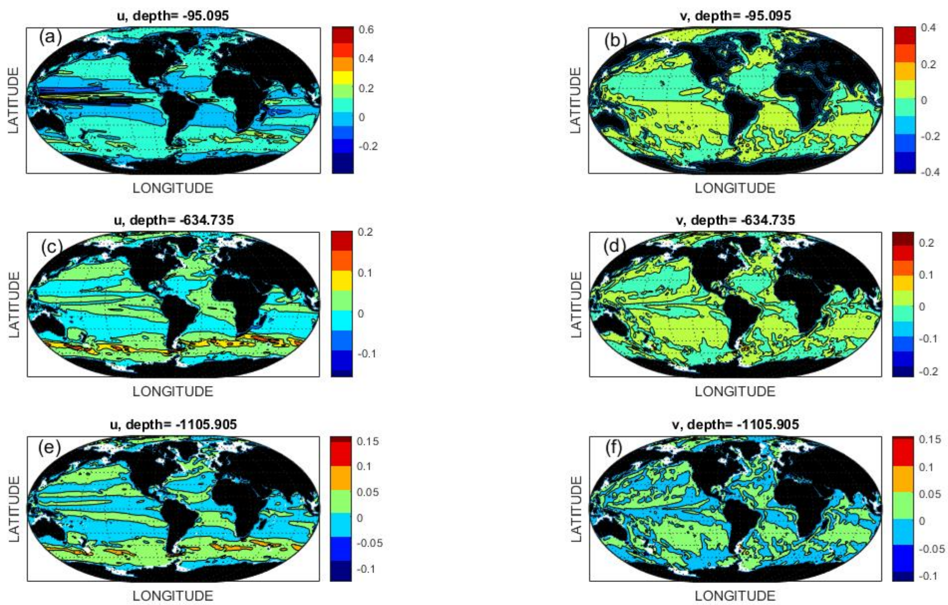

FIG. 1. Time-average zonal velocity (left column) and meridional velocity (right column) at depths (a, b) 95m, (c, d) 635m, (e, f) 1100m. (An expanded version of these charts is contained in the Supplemental Material. Units are m/s.)

are x, y, z. Figs. 1, 2 display the horizontal flow elements, u, v at a variety of depths. (The contouring algorithm used in this paper obscures some small scale features. Enlarged versions of these charts are contained in the Supplemental Material.) The 95m depth shows the conventional features of the near-surface velocity field , including the complex reversing-with-latitude zonal flows near the equator, and the locally intensified patches in the Southern Ocean. The ocean interior meridional flow field at this depth shows the generally equatorward-motion characteristic of Sverdrup balance, in both hemispheres of the Atlantic and Pacific. A very sharp convergence of v is seen at the equator over much of the Pacific and partially so in the Atlantic and Indian Oceans. (Brandt et al. (2008, their Fig. 1) describe the intricate flow field expected in the equatorial Atlantic.) In the meridional flow at 635m, Fig. 1, the vertical persistence of the Sverdrup-balance interiors is clear, with equatorward flow in both hemispheres within the major gyres.

By 1100m several characteristics of the abyssal flows emerge. These include the much greater noisiness of v as compared to u with the latter still displaying a strong tendency toward a series of quasi-zonal jets. A large literature discusses the formation of zonal jets albeit in the ocean primarily

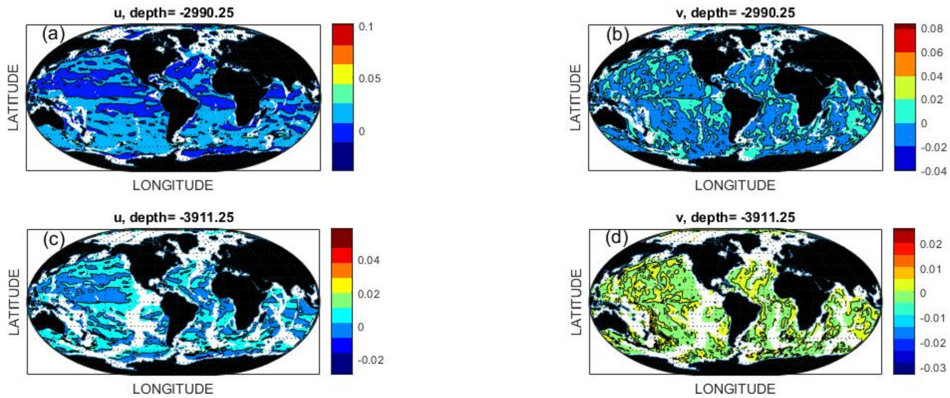

FIG. 2. Time-average zonal flow (left column) and meridional flow (right column) at depths of 3000 (a, b) and 4000m (c,d). (An expanded version of these charts is contained in the Supplemental Material.)

directed at transient features arising from local turbulence (see e.g., the review by Cornillion et al., 2019) .

A foundation of dynamical oceanography is the linearized potential vorticity conservation equation,

$$\beta v = f\frac{\partial w}{\partial z}. \tag{1}$$

Liang et al. (2017) described the time-average vertical velocity fields, w, from a shorter- in-duration ECCO estimate. The fields they found were strikingly complex spatially and with the vertical derivative of w, by implication, being even more so. If Eq. (1) is an accurate description, the corresponding spatial complexity in v and its vertical derivative are expected. A somewhat surprising result is the persistent absence at 1000m in both velocity components of any obvious disturbance from the major underlying topographic features of the mid-ocean ridges. By 4000m (Fig. 2c,d), topographic features (including mid-ocean ridges) and complicated lateral boundaries do intrude directly into the charts with the zonal flow taking on the more noisy elements seen above in v.

a. Velocity Sections-Meridional v

Consider first the meridional velocity across two latitude bands shown in Fig. 3. Characteristically, both show a v-component intensified in a near-surface western boundary current, and a very much weaker interior flow. The latter contains a sign-reversing columnar structure generally below about 1000m, sometimes identifiable with local topography. Such lateral structures in the deep flow field have persisted for decades. What is perhaps surprising is the absence, except in the Southern Ocean (Fig. 4), in the near-surface fields (above about 1000m) of any indication of the presence of such powerful flow and mixing disturbances as the mid-ocean ridges.

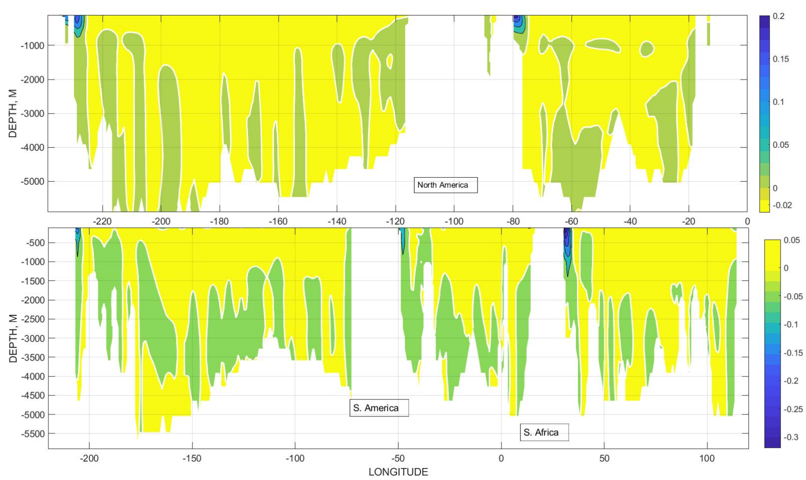

FIG. 3. Meridional velocity at 30°N (upper panel) and 30°S (lower panel) in m/s. Note that the longitude and color scales are different in the two panels. Colorbars are reversed in the two panels so that yellow-orange colors are regions of equatorward flow and thus of opposite sign to greenish areas. Even with 26 years of averaging, a highly structured meridional flow persists at all depths. An intense western boundary current near-surface is just visible in all oceans.

b. Velocity Sections–Zonal u

The character of the zonal velocity, u, orthogonal to the 165°W meridian in the Pacific, is shown in Fig. 5 and displays a rich variety of structures as does an Atlantic meridional section shown there. The equatorial undercurrent is visible (smoothed by the contouring algorithm) in both sections. The only summary statement would be that the flows again remain highly structured after 26-years of averaging.

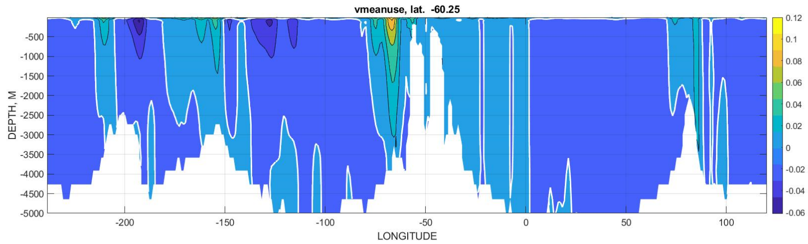

FIG. 4. Mean meridional velocity at 60°S. Zero contour is marked in white. Yellow-orange and light-blue regions here are equatorward flow (positive v). In contrast with mid-latitudes, a strong tendency to barotropic (uniform with depth) flow is conspicuous.

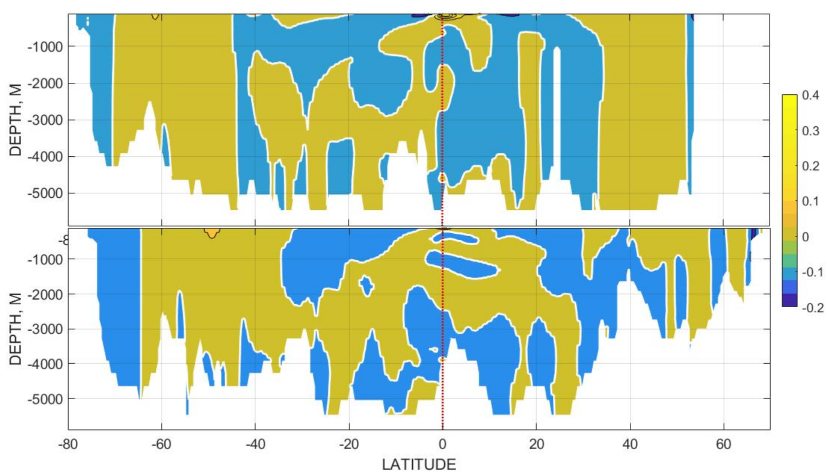

FIG. 5. Time-mean zonal flows along 165°W and 30°W. Latitude scales are identical in the two sections with the white contour denoting zero. Equator is marked by the vertical dashed line.

c. Meridional Overturning Circulation

The zonally integrated meridional transports have in recent years become the focus of intense interest as they represent a very great simplification of the flow field, and particularly as they might directly reflect a changing climate system. Fig. 6 displays the zonal integrals of v in the northern hemisphere at 31°N for the sum of the Atlantic and Pacific Oceans and for the Atlantic

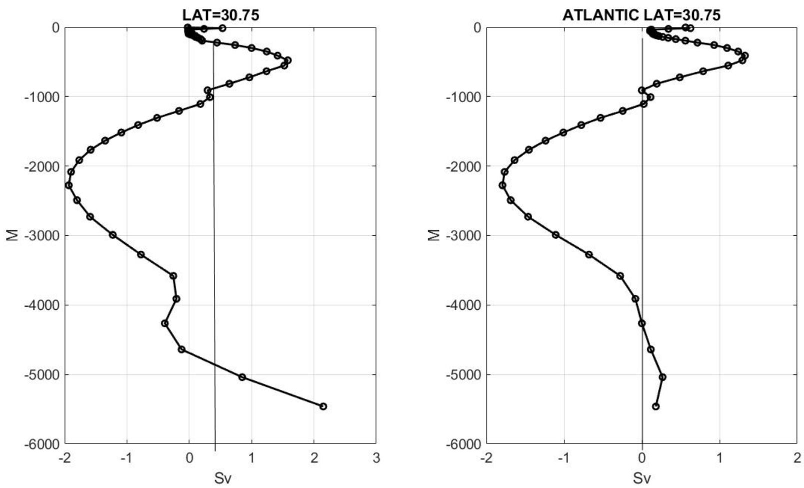

FIG. 6. Zonal integral of the time-averaged meridional velocity, $v(y,z)$, for the global ocean at 31°N (left-panel) and for the same latitude (right panel) in the North Atlantic alone. Both results correspond to conventional expectations.

alone. Both summations correspond to conventional expectations (e.g. Talley, et al., 2011) with the global result showing northward time-average flow above about 1000m and which includes both the Kuroshio and Gulf Stream. Below that, the southward flow consists of the intermediate waters and then a reversal reflecting the northward movement of Antarctic Bottom Water. The North Atlantic profile shows the dominance of the intermediate levels there by North Atlantic Deep Water, but with a much reduced injection, compared to the Pacific, of near-bottom Antarctic-origin waters. (See Roquet and Wunsch, 2022, for references and a commentary on the interpretations of the Atlantic portion).

Corresponding integrals for heat, freshwater, etc. are also readily computed but not shown here. Interpretation of such integrals raises awkward questions, analogous to those in W23, which concerned a one-dimensional physics, as to whether a two-dimensional representation of integrated transports across highly diverse flows has any easy interpretation? Results in Fig. 6 involve integrals across flow fields such as those depicted in Figs. 3 where the flow field—and its underlying physics—varies greatly with longitude and depth.

d. Rossby Number

The log (base 10) of the Rossby number, defined here as $Ro = \sqrt{u(x,y,z)^2 + v(x,y,z)^2}/f(y)L$ based upon a distance of $L = 1^\circ$ of latitude is shown for two depths in Appendix Fig. A4 at 5 and 553m. Apart from the expected singularity on the equator, the Rossby number is less than 0.1 everywhere, including the surface. Charts at greater depths (not shown) all produce smaller values. A robust inference is that the system overall is consistent with geostrophic balance, subject to the caveat that a small Rossby number is a necessary, but not a sufficient, requirement for that to be so (large Ekman numbers or equivalent could preclude the inference). A general westward intensification appears in all oceans. Many Ro values in the Southern Ocean are also O(0.1).

e. Some Generalizations

From this preliminary sketch of the structure of the time-mean flow field, a few globally applicable generalizations appear possible. (1) The 26-year average field remains markedly noisy, particularly in the abyss, where it is subject to strong topographic barriers and unresolved boundary layers. (2) The sub-tropical gyre structures emerge robustly in the two components of flow in the upper approximately 1000m. (3) The three-dimensionality of the flow field precludes a simple explanation from a two-dimensional physics e.g., that as portrayed in Fig. 6. (4) The considerable remaining spatial structures leave an outstanding question: which of them would persist in a much longer time average and which would be suppressed?

3. Thermal Wind

Theory (e.g., Pedlosky, 1982), and the small Rossby numbers seen in Fig. A4 suggest strongly that on the scales of the general circulation (vaguely defined, but here larger than the basic grid scale), geostrophic balance should be maintained almost everywhere. As already noted however, a small Rossby number does not preclude the effects of relatively strong dissipation or eddy fluxes of either sign. On scales smaller than those resolved here exceptions to large-scale geostrophic balance can arise from the effects of balanced eddies, the sub-mesoscale (see e.g., Callies et al., 2016), along-stream pressure gradients in western boundary currents (WBCs), the numerous boundary layers near the sea-surface and near topographic features. With the partial exception of the WBCs, these regions are not resolved in ECCO(v4r4). Numerous textbooks discuss the expected geostrophic balance through the applicability of the thermal wind equations, which are, in local Cartesian coordinates, (x, y, z),

$$f\frac{\partial v}{\partial z} = -\frac{g}{\rho_0}\frac{\partial \rho}{\partial x}, \tag{2a}$$

$$f\frac{\partial u}{\partial z} = \frac{g}{\rho_0}\frac{\partial \rho}{\partial y}, \tag{2b}$$

representing the vertical shear in terms of the horizontal density gradients. f and ρ are the conventional Coriolis parameter and the in situ density. ρ_0 is a constant reference value. Historically, these equations were used with observed hydrographic fields in finite difference form to find the horizontal flow field up to an unknown integration constant. A scale analysis (see e.g., Phillips, 1963, Pedlosky, 1982) shows that this balance is the expected one, apart from boundary layers (including those at the surface and on sea-floor topography including side-walls) and on and near the equator where $f \approx 0$. Separate discussion of the meridional and zonal geostrophic velocities is both convenient and necessary as will be seen.

a. Meridional Thermal Wind

In the meridional component, the thermal wind shear involves a horizontal (in x) derivative of ρ, and the corresponding vertical shear of the velocity field in the state estimate requires a vertical derivative of the northward velocity component v. Anywhere adjacent to a topographic feature, disagreement is expected between the thermal wind shear and $\partial v/\partial z$ both because unresolved boundary layers of several types are anticipated there, and from the simple centered finite differences being used here. As will be seen however, over the great bulk of the ocean, quantitative agreement is found. In practice, use of simple centered-differences appears to produce as much similarity between the two fields as does use of the differencing stencil of the model (not shown).

Consider first a single zonal section at 30°S (Fig. 7) spanning all longitudes, some of which are land. Visually, the two patterns of the two sides of the thermal wind equation differ in small details, many attributable to the finite differences taken in the presence of complicated topographic boundaries. The median difference is 2×10^{-7}/s. Vertical profiles of the thermal wind shear (computed from ρ) and $\partial v/\partial z$ at three longitudes are displayed in Fig. 8. (The separate centered differences in the vertical and horizontal render the effective topography as visually somewhat inconsistent.) A comparable display for 60°S is in Appendix Fig. A7—and showing a greater visual difference between the two calculations.

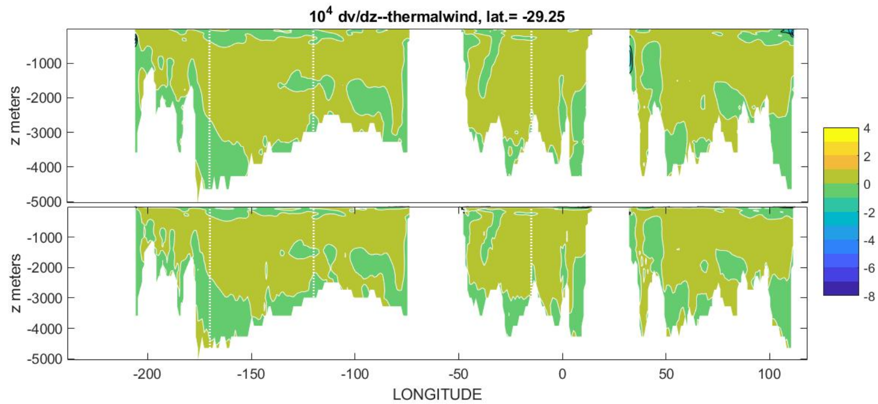

Fig. 7. Thermal wind shear from ρ (upper panel) and dv/dz (lower panel) directly from the estimate at 30°S both multiplied by 10^4. Topographic details appear to vary owing to the way in which $x-$ and a $z-$derivatives are taken in different directions relative to the various boundaries. A general similarity exists with small deviations, most commonly in the very upper ocean.

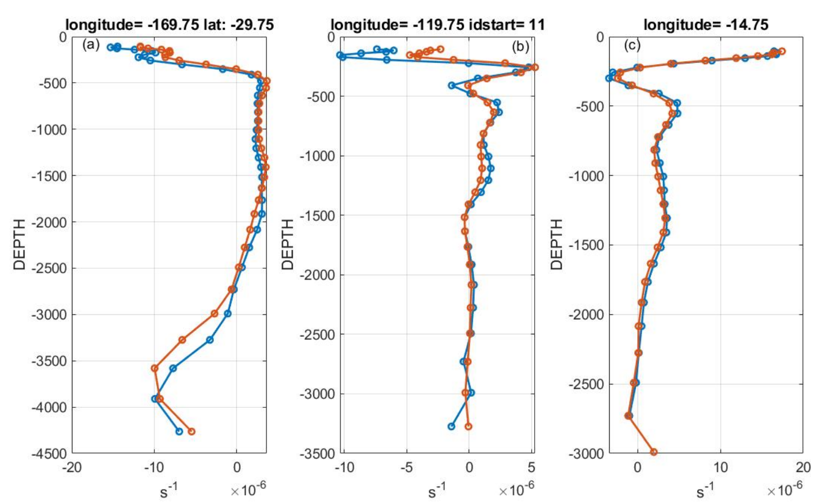

Fig. 8. Profiles with depth of the thermal wind shear and of $\partial v/\partial z$ at three Pacific longitudes 169°W, 190°W, -200°W at 30°S.

To obtain a quantitative measure of the degree of similarity of the two fields, consider at each horizontal point the two vectors corresponding to the discrete rendering of $\mathbf{a} = \partial v\left(x, y, z_j\right) / \partial z$ and $\mathbf{b} = g/(f\rho_0)\partial\rho\left(x, y, z_j\right) / \partial x$. The projection $p_v = \mathbf{a}\cdot\mathbf{b}/\left(|\mathbf{a}|\,|\mathbf{b}|\right)$ is the cross-correlations of the vertical structures of the thermal wind shear and the vertical derivative of v in the model. But as the system is here being treated as deterministic, the outcome of the numerical cross-correlations will be referred to as the "normalized projection" of the two fields (or just the "projection") with maximum magnitude 1. From the figures, e.g. Appendix Figs. A6, A8, a variety of deviations in the upper few hundred meters are apparent and the projections are taken below 200m.

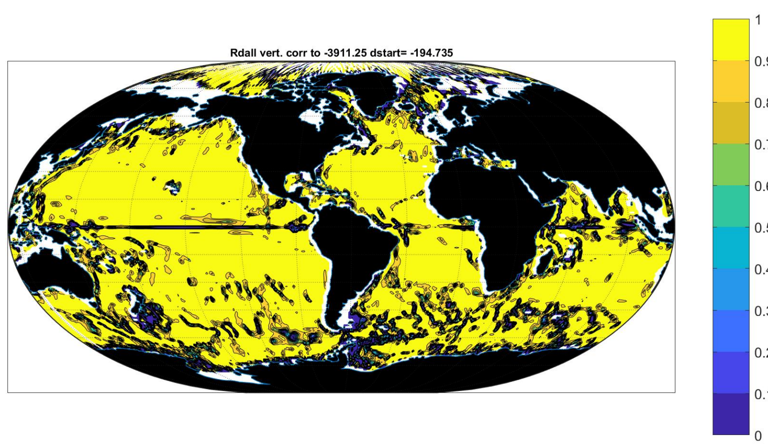

FIG. 9. Global values of the projection, p_v, of the vertical structure of the meridional thermal wind shear onto the vertical shear, dv/dz from 200m depth downward to 4000m. Apart from the Southern Ocean and the immediate vicinity of the equator, the two fields are very similar everywhere.

The magnitudes (all positive) of p_v are shown in Fig. 9) and generally exceed a value of 0.8. Reduced values occur where anticipated—including boundary regions on the African coast and elsewhere, high northern convective regions of the North Atlantic, the Kuroshio extension, and in the Southern Ocean generally. Regions of deviation from large-projections are generally the result of failure of the thermal wind balance in the near-surface (down to about 200m), as can be seen e.g., in Figs. 8, A6.

Thermal wind balance of the meridional flow, v, appears to be a good general oceanic description with the exception of the equator and parts of the Southern Ocean—both regions where a failure would be expected based upon the basic physics of the vanishing of f in the former, and in the latter of the topographic pressure balances of quasi-zonal flows (e.g. Wilson et al., 2022). Adjacent to topography, the situation is somewhat obscure, as both a failure of boundary layer resolution, and numerical issues of differentiation of topographic, partially filled, grid boxes occur.

Behavior in the Southern Ocean is interesting—and the physics there has been the subject of much discussion (see e.g., Wolfe and Cessi (2010), Vallis (2017) and their numerous references).

b. Meridional Lines–Zonal Thermal Wind

Local thermal wind-shear balance is much more fragile in the zonal flow, u, than it is in the meridional component, v. The literature on zonal jet formation suggests a much greater sensitivity of zonal mean flows to the eddy field than is the meridional component. A strong tendency toward zonal flows occurs, especially in the Pacific Ocean, both in the variability (not shown) and time-averages of varying duration. See for example, Berloff et al. (2009) or Chen et al. (2015); both are idealized analyses of turbulent interactions and divergences leading to zonal jets. The edited volume by Galperin and Read (2019) discusses the subject in the wider context including the atmospheres of both of the Earth and of the giant planets. Cornillion et al. (2019) review much of the oceanographic observational evidence (although no true time-average was available). An example is the regional South Atlantic study by Hogg and Owens (1999). Zonal flows are potentially generated by a variety of detailed turbulent mechanisms and interactions with the background velocities.

In a dissipationless ocean without meridional barriers, zonal flows are free solutions and will also tend to appear if western and eastern boundary currents can absorb or provide the incoming or outgoing flow. To the extent that deviations from geostrophic balance occur in the present state estimate, they would arise from the parameterizations used to represent the unresolved eddy fields and boundary layers. Fig. 10 displays the zonal thermal wind shear and $\partial u/\partial z$ along 165°W. Profiles of the two fields at three latitudes along this longitude are in Fig. 11. Because of the equatorial singularity, $f\partial u/\partial z$ is computed from Eqs. (2). The two fields range from showing near-coincidence to considerable differences. Projections will, in any case, be dominated by the upper 500m where the shear is greatest.

Apparent regional deviations from thermal wind shear as an accurate determinant of $\partial u/\partial z$ can arise from at least two causes: (1) low-frequency time-variation in a particular area renders the temporal average relatively far from a true value. (2) Strong unresolved eddy divergence effects are present, rendered in the state estimate through the parameterized values. Spectra of low-frequency variability is likely different for u, ρ. Appendix Fig. A3 shows the logarithm of the annual average standard deviation for speed in the surface layer about the 26-year mean for each grid point and which produces, as is well-known, a very strong regional dependence.

A global chart of the profile projections, p_v, is in Fig. 12. In contrast to Fig. 9, the result displays a series of dominantly zonal bands of reduced projection values. The summary statement might be that although thermal wind balance of the zonal flow is a good approximation over much of the ocean outside the Southern Ocean, regions of measurable deviation do exist with a dominantly zonal character at mid- and low-latitudes. (A layer-thickness weighted projection (not shown) necessarily produces larger values as the greatest deviations between the two profiles is in the upper ocean.)

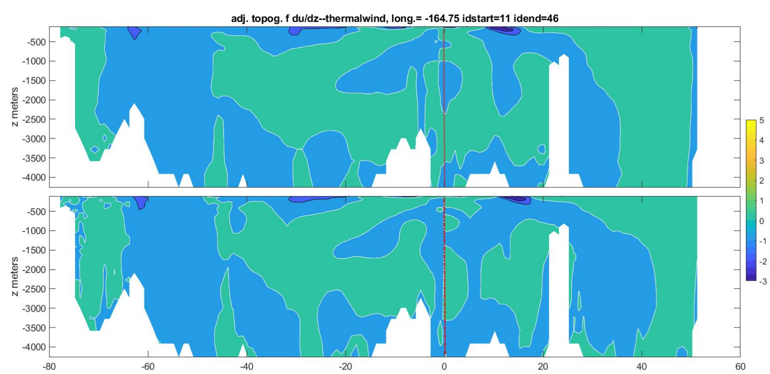

Fig. 10. Upper panel is f times the thermal wind shear along 165°W and lower panel is the corresponding vertical derivative of the model $u(x,y,z)$. Qualitatively great similarity is apparent but with small systematic offsets in the deep water.

c. *f/h Contours*

One of the robust implications of a steady geostrophic flow over topography is that the streamlines should follow the contours of f/h (e.g. Vallis, 2017). With the complicated topography, $h(x,y)$, (see the Appendix, Figs. A1, A2) much regional complexity exists. The strong latitude dependence

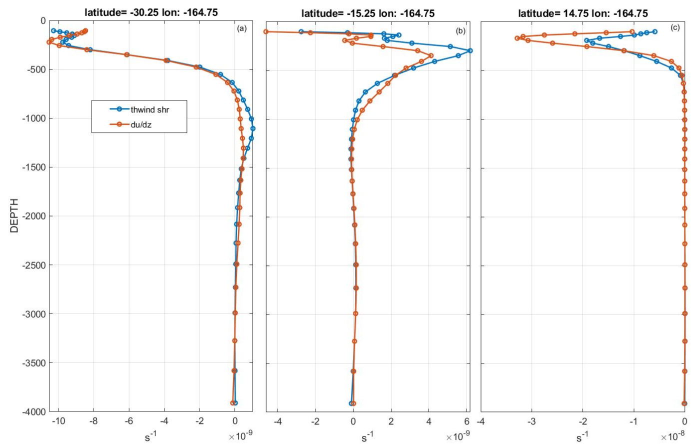

FIG. 11. Profiles of thermal wind shear and $\partial u/\partial z$ along 165°W. Strongest deviations between them tend to occur above about 1000m depth. Other profiles can be found in the Appendix.

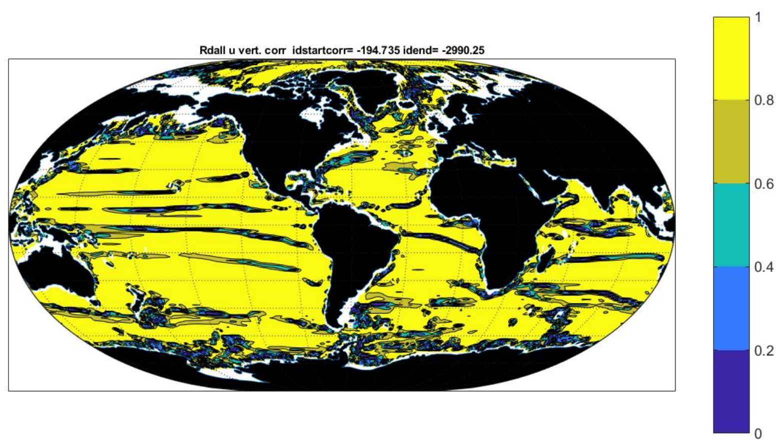

FIG. 12. Projection, below 200m of the zonal component of thermal wind shear profiles, onto the profiles of $f\partial u/\partial z$ directly from the state estimate. Note the zonally-banded structure here is mostly absent in the meridional flow component. Numerous reduced values contrast with the results for the meridional vertical shear.

of f leads to a corresponding tendency toward zonality at low latitudes and over much of the tropical Pacific.

One example of an exception, noticed long ago, is the region of closed contours in the Argentine basin. de Miranda and Barnier (1999) discuss studies of what is called the Zapiola Drift, but which is a highly regionalized result. Note the intensified flow there in e.g., Fig. 1c,d. Many other regional analyses are obviously possible.

d. *Reference Levels*

In the period of classical oceanography almost the only general circulation estimates could be made using the thermal wind shear—converted to absolute velocity by assuming a deep "level-of-no-(horizontal) motion", or "reference level." Recent observational tools produce direct estimates of absolute values of u,v (altimeters, floats, improved meteorology combined with higher order dynamics,...) and a reasonable question is whether some simple distribution exists for levels of minimum speed and/or velocity components?

From the 26-year average, the answer to the question of "where is the depth of minimum flow?" is a spatially complicated field. Even when smoothed over 10° degrees of longitude and 5° of latitude, the result for the net speed shows (Fig. 13) a complicated pattern. A gross generalization is that minimum speed depths in the tropics tend to be between 500 and 1000m, and at high southern latitudes, generally lie close to the seafloor, but with numerous exceptions. The zonal averages in water depths exceeding 3000m in Fig. 13 show an overall trend upwards from the southern towards the northern hemisphere with a secondary minimum at northern midlatitudes.

In the North Atlantic reference levels-of-no-motion for v have commonly been chosen near 1500m (e.g., Leetmaa et al., 1977) and these present results suggest a value of smallest speed nearer 2000m there.

4. Spirals

Velocity spirals enter into discussions of oceanic flow under at least three circumstances: (1) in the Ekman (1905) layer; (2) in large-scale geostrophic flows as the beta-spiral (Stommel and Schott, 1977); (3) the surface manifestation in the submesoscales of Munk et al. (2000). For present purposes, (3) is not relevant. The question of the extent to which the time-averaged state estimate is at least consistent with either of the remaining descriptions is worth asking in the pursuit of global-scale quantitative descriptors. (An apparent Lagrangian particle spiral in the Southern Ocean has been described by Tamsitt, et al., 2017, but the discussion here is confined to Eulerian mean values.)

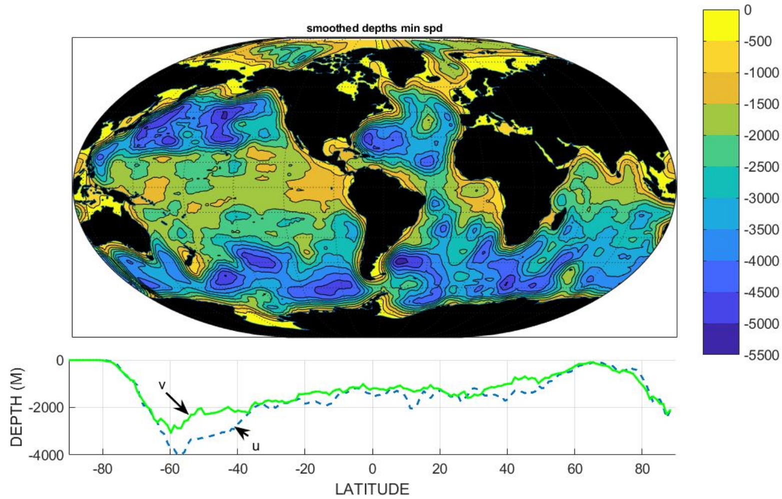

FIG. 13. (Map, upper panel) Depth of the minimum speed in the water column, smoothed over 10 degrees of longitude and 5 degrees of latitude. Tropical and high latitudes do differ but each band has numerous structures. Only water depths greater than 3000m were included. (Lower panel) Global zonal average of the depth of minimum flow shown for u, v separately.

a. Near-Surface Ekman-like Spirals

The ECCO(v4r4) model lacks the near-surface resolution required to depict the complex processes, including the energetically dominant surface waves, Langmuir cells, Stokes velocities, seasonal and night-time convection, and other flows present in and near the upper boundary of the ocean. The literature, dating back to 1905 and Ekman's paper, postulates the existence of an Ekman layer in an unstratified, uniformly rotating fluid. Price et al. (1987) discuss observations and realism issues. In a notation almost identical to theirs, the classical Ekman layer takes the form,

$$[u(z'), v(z')] = V_0 \exp(-z'/D_E)\,[\cos(\pi/4 - z'/D_E), \sin(\pi/4 - z'/D_E)] \tag{3}$$

$$V_0 = \frac{\tau}{\rho_0 (A_v f)^{1/2}}, \quad D_E = \left(\frac{2A_v}{f}\right)^{1/2}$$

where τ is the mean wind-stress, however defined, A_v is a vertical eddy viscosity, and D_E is the Ekman depth. $z' = 0$ is defined such that $(u(z'), v(z'))$ lies at 45° to the right or left (northern/-

southern hemisphere). Some of the consequences of stratification and heating are described by Price et al., (1986) and by later authors. With layer thicknesses of 10 meters between the surface and 100m, resolution of an Ekman layer is possible (Price et al., 1987). McWilliams et al. (2012) analyze numerically some of the complex, intense, surface wave and Langmuir circulation effects, and Shrira and Amehla (2020) discuss some consequences of time-dependent viscosity/dissipation. The ECCO near-surface boundary layer model is based on that of Gaspar et al. (1990) and which includes stratification. These papers and numerous related ones mean that finding a useful wide-spread description of the expected upper-level current structure in the mean-state is not necessarily possible.

Perhaps surprisingly, near-surface spirals are found in the ECCO(v4r4) time-average—spirals whose hemispheric dependence on the sign of the Coriolis frequency is consistent with that expected for the classical Ekman layer of an unstratified, otherwise resting, ocean.

Consider first Fig. 14 which shows hodograph plots with depth z at four locations along the 165°W meridian. A typical behavior is the change from Fig. 14a of a reversal of sign across the equator of the sense of the spiraling velocity field with depth in (c) and (d). The spiral construct fails at a distance of 1/4° from the equator—the nearest grid points. Note that in panels (a), (c) the top layer (5m thick) does *not* reproduce the classical Ekman layer result having a maximum speed at the surface, whereas (d) does show that result.

A simple test of a spiral-like behavior is used here by computing the sign of the turning with depth in the hodograph at each lateral grid point. Ekman-like behavior appears, producing a counter-clockwise spiral in the Southern Hemipshere (increasing, positive angular sign with depth), and a clockwise spiral (increasingly negative sign angle sign with depth). A measure of consistency—quality of the fit—within the upper layers is computed from the sign of the change from one layer to the next in the top 5 layers. A value of ± 2 means complete consistency, and a value of ± 1 implies a single reversal between two of the layers, but with an overall consistently spiral-like behavior. Results are shown in Fig. 15. The most common cause of a reduced magnitude quality value is the occurence of the maximum in layer 2 rather than in the top-most layer (as seen in Fig.14a,c). Nonetheless, the spiral structure remains. With some minor regional inconsistencies, generally near boundaries and including parts of the Mediterranean, the expected different signs in the two hemispheres is pronounced. Generally speaking, the fit is best far from oceanic boundaries. That

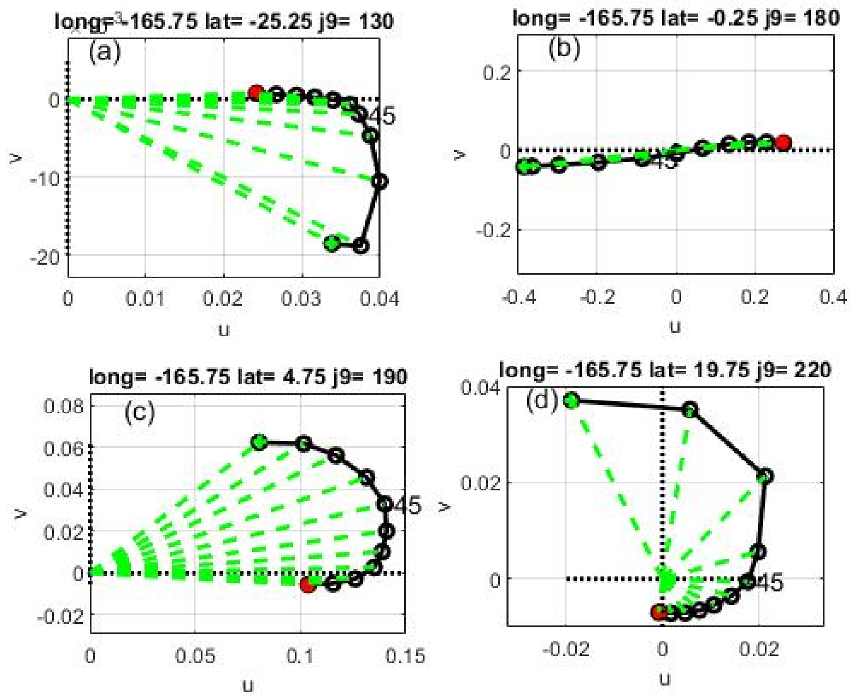

FIG. 14. Sample hodographs along 165°W in the central Pacific Ocean at different latitudes. Units are m/s. Green dot denotes the value (5m layer) nearest the surface, and the red dot the terminal value at a depth of 105m. South of the equator (a), movement is counter-clockwise with depth (here the velocity magnitude is largest in layer 2). (b) Hodograph at 0.25°S showing the expected failure of a simple Ekman-like spiral on and near the equator. (c,d) show clockwise spirals in the northern hemisphere at 4.75°N and 19.75°N. (c) has a clear spiral, but one of increasing magnitude with depth down to about 50m. (d) Spiral has the property that the top layer has the strongest flow.

the underlying physics is Ekman-like is a reasonable inference, albeit the behavior of the underlying turbulence remains to be understood and further exploration involves the vector wind-field.

The estimated e-folding scale depth, D_E, is determined from a least-squares fit to the logarithm of the hodograph from Eq. (3) analogous to the procedure in W23. Compared to the sense of rotation, it is less spatially stable, even with a 26-year average, near-surface. Again the question arises of whether a 26-year average is of sufficient duration to provide a stable mean? The fit was made for layers 2-10, omitting the top layer. The physics may well be that of an Ekman layer—but here it is just a readily computed reparameterization of the physics of the uppermost layers. Appendix Fig. A5 displays the equivalent value of A_v determined from D_E although its significance remains obscure and the result is spatially very variable. To the extent the physics is indeed that of Ekman layers, the corresponding patterns of injection of energy to the circulation are discussed by Roquet et al. (2011).

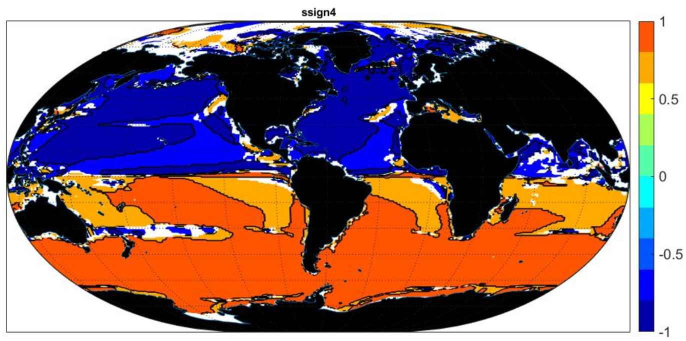

Fig. 15. Orange-red regions display a counter-clockwise behavior in the flow of the surface layers, and the blue areas are correspondingly clockwise, both as expected from Ekman-like dynamics with a sharp change across the equator. Values represent a measure of the quality of the spiral fit. Darker colors indicate a stronger fit. Those less than $|1|$ exhibit some inconsistencies, but spiral direction is, overall, as indicated by the sign. Blank regions of failure are associated with eastern boundaries and quasi-zonal bands, especially east of Australia.

b. Beta-Spiral

The expected turning of the time-averaged flow with depth in the geostrophically balanced interior was explicitly introduced by Stommel and Schott (1977) and elaborated in several later papers e.g., by McDougall (1995) for the presence of lateral mixing. For present purposes, the discussion in Olbers et al. (2012, P. 153+) of the formulation in geographic coordinates is adequate.[2]

In a perfect fluid in steady-state, conservation of density can be written,

$$u\frac{\partial\rho}{\partial x}+v\frac{\partial\rho}{\partial y}=-w\frac{\partial\rho}{\partial z}, \tag{4}$$

[2]In this context, the equations are usually written in terms of isopycnal or neutral surface coordinates instead of the z coordinate, but the latter is more stable in a geographical-coordinate model output.

and with conservation of planetary potential vorticity leads (Olbers et al., 2012, their Eq. 5.67) to,

$$u\frac{\partial}{\partial z}\left(\frac{\partial\rho/\partial x}{\partial\rho/\partial z}\right)+v\left[\frac{\partial}{\partial z}\left(\frac{\partial\rho/\partial y}{\partial\rho/\partial z}\right)+\frac{\beta}{f}\right]=0 \tag{5}$$

and which perhaps carries to its outer limit the present requirement of a "simple" relationship. Schott and Stommel (1977) produce a construct (their equation 1.4) for the rate of turning of the hodograph as,

$$\frac{\partial\theta}{\partial z}=\frac{g}{f\rho\left(u^2+v^2\right)}\left(w\frac{\partial\rho}{\partial z}-\frac{\partial\rho}{\partial t}\right) \tag{6}$$

for a perfectly geostrophic flow. $\partial\rho/\partial z<0$ for static stability and, by assumption, the time-derivative of ρ vanishes in the time-average. Thus the sign of w determines the direction of turning. As long as a meridional component exists, the linear vorticity conservation equation implies w is non-zero. Results in Liang et al. (2017) show a very noisy $\partial w/\partial z$.

Instead of attempting to determine the predicted rate of turning from Eq. (6), the simple question is asked whether evidence exists for interior spirals approximately encompassing the main thermocline? The answer to this question is "no": spirals do exist in many places (Fig. 16, but many others display a depth dependence closer to a straight line and others have no readily discernable analytic structure. Attempts to fit spirals over a depth range of 550 to 3000m produced a complicated spatial dependence (Fig. 16). Deviations from a simple spiral are expected from complexities in w, vertical changes in lateral kinetic energy, along with any generic deviation from perfect geostrophic balance.

The $\beta-$spiral thus does not produce any simple generalization about the flow field—consistent with the spatial noisiness of v,w. A significant fraction of the ocean, but mainly in the Southern Ocean, exhibits a linear trend of the hodograph with depth, with the sign of the linear trend varying rapidly (not shown).

5. Where are the Thermocline and Pycnocline?

A centerpiece of dynamical oceanography is the theoretical explanation of the "main thermocline" in the upper ocean where the vertical temperature derivative is strongest, usually corresponding to maximum derivatives in salinity and density as well. That structure is normally distinguished from the seasonal thermocline which waxes and wanes over the year (see Talley et al., 2011, for a

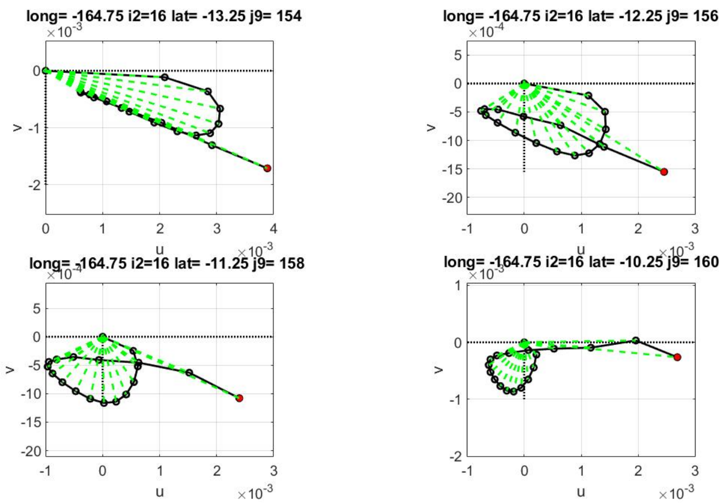

FIG. 16. Beta-spiral hodograph plots showing a variety of linear and spiral-like features along 165°W. Again, starting depth is marked in green, ending depth in red. Latitudes are 25°S, 0°,5°N, 20°N (panels left to right, top to bottom). Depth range is 550 to 3000m.

generic description). In the wider literature, definitions of the thermocline depth are vague—being replaced by various theories in different models and producing depths of the order of several hundred to about 1000m (see for example, Pedlosky, 1996; Huang, 2010). A useful question is whether *a* thermocline depth can be defined in a time-average ocean?

The gist of W23 however, is the implication that temperature and salinity distributions can be very different—largely as a result of distinct boundary conditions at the ocean top and bottom, and the three-dimensional flow field. As discussed in the various thermocline theories, the dynamically important physics of the circulation lies with the density distribution and not with T,S separately. For that reason, only the geographical structure of the *pycnocline* in the time-average is depicted here.

Consider as examples Figs. 17, 18 for $\partial\rho/\partial z$ along 30^oS, 30^oN across all ocean basins. A 60°S section can be seen in the Supplemental Material. Visually, it is not easy to define a particular vertical scale characterizing the vertical rate of change. Generally speaking, vertical rates of change of density are largest in the region above 100m—usually considered the domain of the seasonal thermocline and of the Ekman and other boundary-layers. Evidently, the averaging process leaves a time-mean near-surface thermocline, interpretable as owing to the net fluxes of heat, moisture, and momentum. In the regions below 100m, a general, near-exponential decline in the derivative occurs, but a single, ocean-wide characteristic depth is not visually obvious.

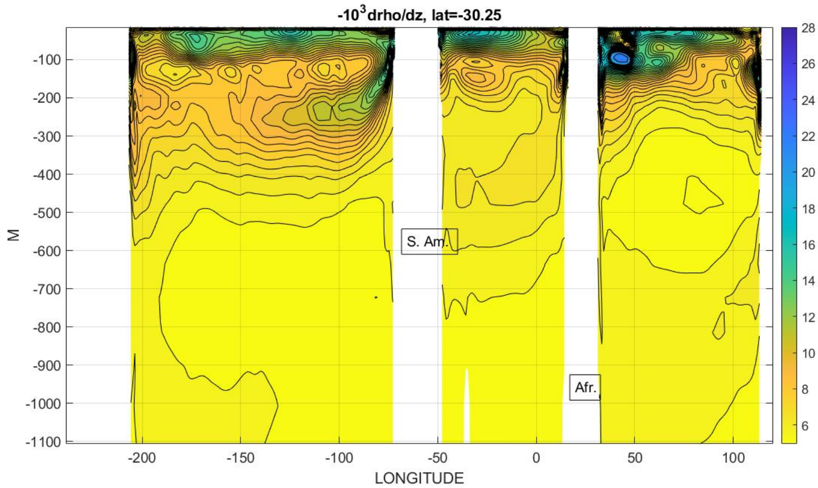

FIG. 17. 10^3 times $\partial\rho/\partial z$ at 30^oS. The sign is rendered so that the derivative is positive downward. Contour separation is numerically constant. Density is the in situ value.

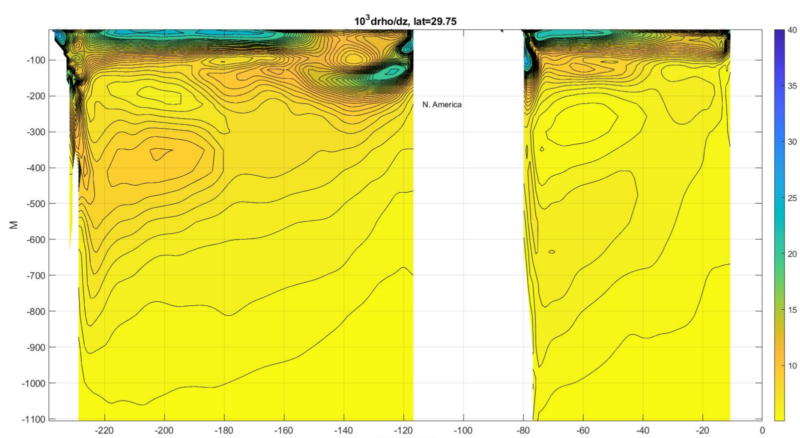

FIG. 18. 10^3 times the z derivative of in situ density at 30^oN. The sign is rendered so that the derivative is positive downward.

6. Discussion

From a focus on the flow field, the quest for universal, simple, properties and patterns in an estimated 26-year time-mean ocean circulation produces a number of results that characterize this specific time average circulation and provide a basis, both qualitative and quantitative, for comparison with any other estimate of a time-average. A major, overall, description is the survival of much structure, particularly in the horizontal, despite the multi-decadal averaging time. Whether much longer, hypothetical, avergaging times would produce and further great simplification remains unknown. Some properties and patterns nonetheless do emerge: (1) Over the abyssal ocean, an exponential fit in z to the potential density field is found (W23 and Rogers et al., 2023) and slowly varying with horizontal position scale height. (2) Apart from the equatorial region, the Rossby number based on a 110km scale, is small—less than about 0.1 everywhere. (3) Consistent with small Rossby number (a necessary but not sufficient condition), the meridional thermal wind shear is in geostrophic balance over most of the water column below about100m, with the Southern Ocean displaying apparent ageostrophic results above about 500m. Zonal flow thermal wind balance tends to be violated at greater depths in zonal bands. (4) Near-surface, and consistent with the implications of Ekman layers, spirals of clockwise (northern hemisphere) and counter-clockwise (southern hemisphere) turning with depth are found almost everywhere (Fig. 15), although departures from a strict surface maximum flow do exist widely and the vertical scale height is spatially variable. (5) A single simple definition of the thermocline/pycnocline depth is not obvious. (6) The issue of the dynamical equations governing the time-average circulation can be answered partially as being those for quasi-geostrophy in the meridional velocity except for the Southern Ocean and in the zonal velocity too with the addition of a number of quasi-zonal strips where deviations from balance exist. (7) The tentative answer to the question of whether spatial and temporal averaging are interchangeable (a hypothesis of simplification) is apparently negative, with the spatially complex influence of the sidewall and bottom topography boundaries emerging as strong signals in the time-average. Any hope that a multi-decadal average would produce a simplified ocean circulation is only partially borne out. Many more descriptors of the time-mean ocean circulation are possible. An example is Buzzicotti et al. (2023) for the spatial scales of kinetic energy.

A final caveat to all of the above is that the ECCO(v4r4) state estimate is is indeed only an *estimate* of the ocean circulation—albeit one that largely fits all of the global scale data constraints of the open ocean (listed in various of the references), and simultaneously is a full solution to a consequently adjusted, free-running, oceanic GCM. An old rule-of-thumb for analysis of

5	15	25	35	45	55	65	75	85	95	105	116	127	140	154	172	195	223
257	300	351	410	477	553	635	722	814	910	1007	1106	1206	1306	1409	1517	1634	1765
1914	2084	2276	2491	2729	2990	3274	3581	3911	4264	4640	5039	5461	5906				

TABLE A1. Depths (meters) of the layers in the ECCO(v4r4) state estimate

time-series is that recalculation is worthwhile when the duration doubles in length. The present time-estimate will grow incrementally with the passage of time. But in the interim, the model should improve, resolution should increase, and more data will be better understood.

APPENDIX

Topography, Variance, Eddy Viscosity, Boundary Layers

Layer Depths, Topography, f/h

In the interests of simplicity, layer depths in the text are sometimes rounded to the nearest 10 or 100m. Thus for example, 2990m is referred to as 3000m.

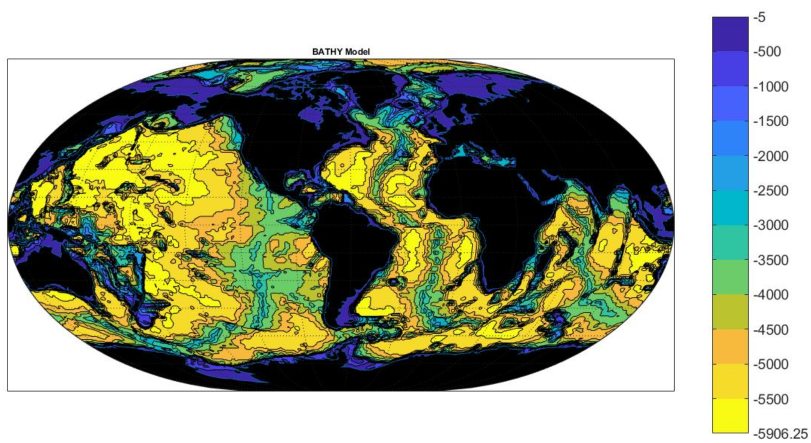

FIG. A1. Bathymetry, h, used in the state estimate model. Depths in meters. The complexity effects the flow field out to the longest time-scales. Those features will not disappear with temporal averaging.

The topographic complexity (Fig.A1) under the strong latitude dependence of f produces contours of f/h (Fig. A2) that tend to be zonal at low-latitudes, but with much structure at mid- and high-latitudes.

Temporal Standard Deviation, Speed

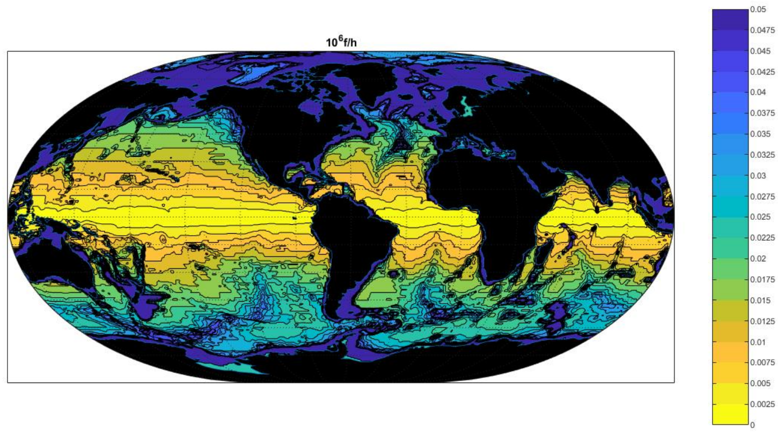

FIG. A2. $10^6\,|f/h|$, units 1/(m s). The overlay of the meridional dependence of f and particularly its zero value on the equator simplifies the topographic structures, but any geostrophic flow attempting to follow f/h contours is still subject to the variations in h alone.

The standard deviation of the surface speed as inferred from annual average of u, v is shown in Fig. A3. High values appear generally where expected including the western boundary currents, the equatorial regioins and the Southern Ocean. A similar calculation for temperature (not shown) displays markedly larger variability in the northern North Atlantic Ocean, and is presumably a consequence of sensitivity to variations in convective intensity, coupled with the long baroclinic adjustment times at high latitudes (e.g., Anderson and Gill, 1975).

Boundary Layers

Most of the available global-scale data concern the oceanic state lying outside the numerous boundary layers expected in the ocean at all surfaces including bottom topography, the sloping sidewalls, and the surface physics, and which are not resolved by the state estimate. The ECCO system, with the existing resolution, is an inverse problem in which parameterized (by the coarse resolution) boundary values are calculated from the observed interior solution. The Gulf Stream and other western boundary currents provide one example: these currents are not dynamically resolved in the state estimate. But if the interior flow is forced to consistency with resolved structures and it drives a boundary current mass or volume transport, e.g. through a Sverdrup-relation, then the interior property structures and transports of the system may well be accurately determined without complete dynamical consistency in the boundary layers. (For reference, the

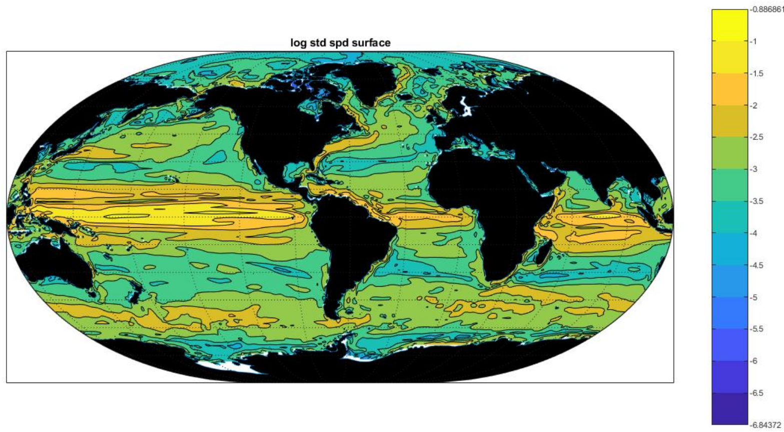

FIG. A3. Logarithm of the standard deviation, m/s, at the surface, based upon 26 1-year averages. High latitude North Atlantic Ocean is conspicuously noisy with secondary maxima apparent e.g., in the Kuroshio and Gulf Stream extensions. Column total patterns are similar but with relatively larger values in the Southern Ocean. Quasi-zonal bands of low and high variance are conspicuous.

topography, h, and boundaries as employed in the estimate can be seen in Fig. A1 along with the Table of model layer-interface depths. Fig. $A2$ shows the corresponding values of f/h where f is the Coriolis parameter.) Yet finer-scale boundary layers required to satisfy the no-flux and no-slip conditions at topography are implicitly parameterized without, it is assumed, doing violence to the data-constrained interior solution.

Rossby Number

Fig. A4 displays the logarithm of the estimated Rossby number at two depths. It tends to be very small at these and all other depths apart from the equatorial singularity.

Equivalent vertical eddy coefficients

The equivalent vertical eddy coefficient A_v corresponding to the Ekman spiral is shown in Fig. A5 and is markedly variable.

Thermal Wind Shear Profiles

Some of the deviations from perfect thermal wind balance in v at 60°S can be seen in Fig. A6. Fig. A7 shows the complete zonal structure.

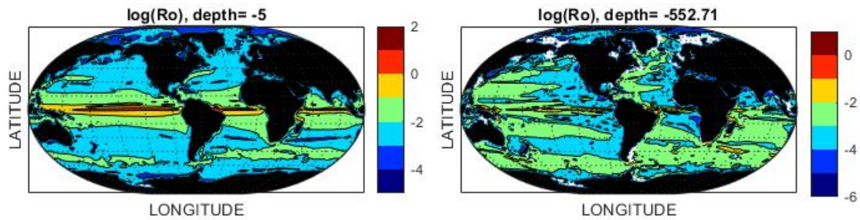

Fig. A4. Log_{10}(Rossby number) at 5m (left panel) and at 550m (right panel).

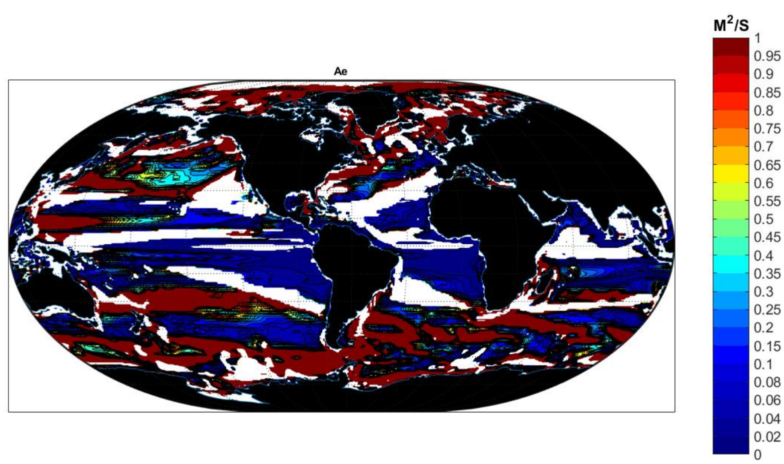

Fig. A5. Equivalent vertical eddy-coefficient A_v determined from the near-surface spiral. Units are m^2/s. In the blank areas, no estimate could be made that passed the ordinary significance test for the fit. Note that although some overlap exists with the structures in Fig. 15 they are not the same because the measures of fit differ.

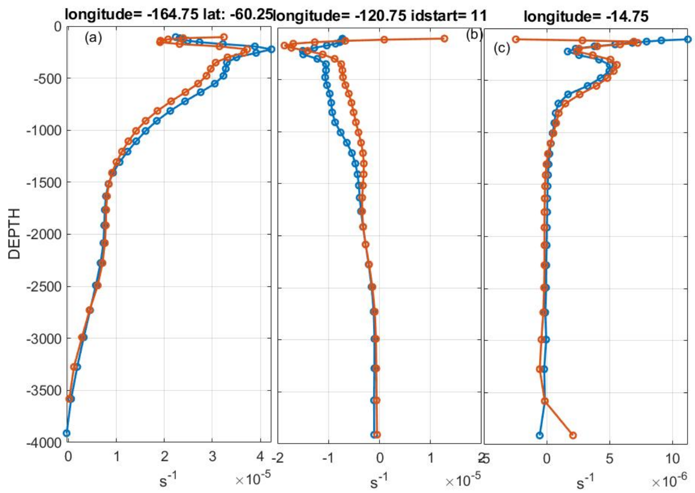

564 FIG. A6. Profiles of the meridional thermal wind shear at 60°S at three longitudes, 170°W, 50°W, 15°W
565 showing that the major differences occur in the upper ocean.

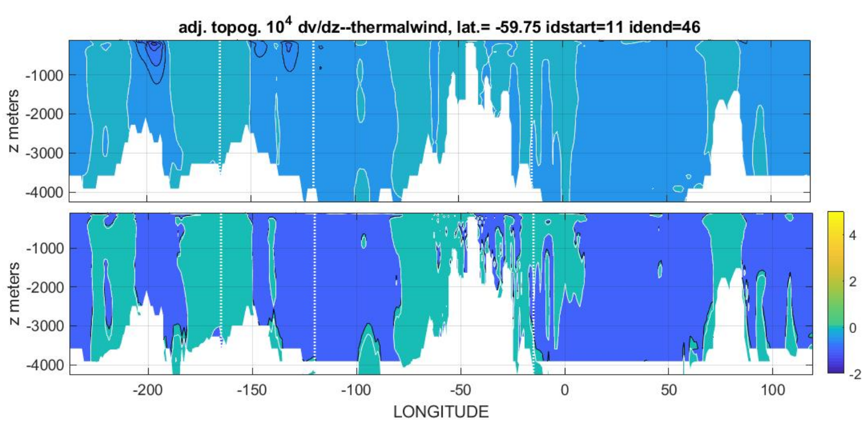

568 FIG. A7. 60°S thermal wind shear (multiplied by f from the density field (upper panel) and dv/dz (lower
569 panel). Difference between the two fields is greater here in the Southern Ocean than is seen at middle latitudes
570 with a slight systematic difference in the southward going regions. Centered differences exaggerate the structural
571 differences of apparent topography.

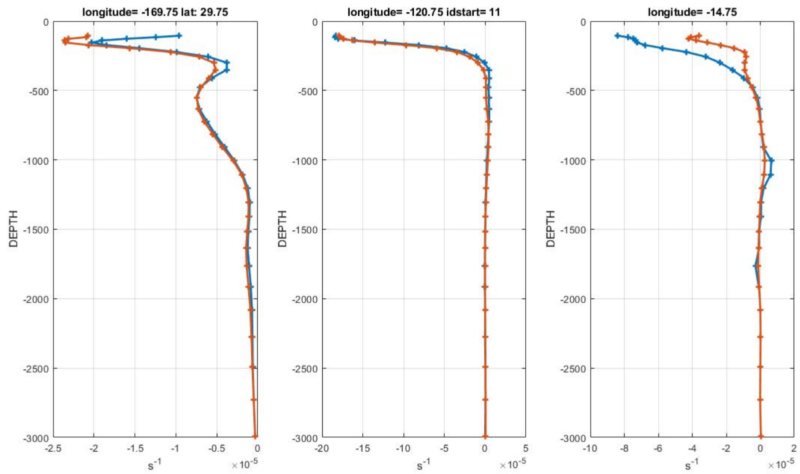

Fig. A8. Thermal wind profiles for velocity, v,profiles along 30°N in the three longitudes.. Left-most and center panels are in the Pacific Ocean (at 169°W, 121°W) and the third is a North Atlantic profile at 15°W.

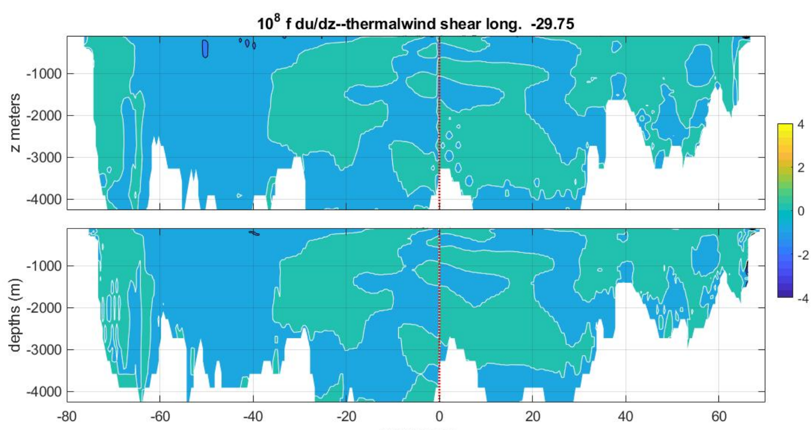

Fig. A9. Thermal wind shear (upper panel) and $f\partial u/\partial z$ (lower panel) along 30°W in the Atlantic, both multiplied by 10^8.

Acknowledgments

This work was made possible only because of the collective efforts of individuals who obtained and quality-controlled the extremely diverse near-global data sets, and the efforts of the ECCO consortium members who produced the global dynamical estimates. They are too many to name individually, but I am grateful nonetheless for their work. Self-supported, but based upon the ECCO Project products.

Conflicts. The author has no conflicts of interest.

Data Availability Observational data were used only indirectly this paper. The ECCO state estimate as well as the underlying model and the observational data used for it can be found on the ECCO JPL/NASA website: https://ecco.jpl.nasa.gov/drive/files/Version4/Release4.

References

Anderson, D. L. T., and A. E. Gill, 1975: Spin-up of a stratified ocean, with applications to upwelling Deep-Sea Res., 22, 583-596.

Berloff P, Kamenkovich I. 2019. Dynamics of baroclinic multiple zonal jets. In Zonal Jets. Phenomenology, Genesis, and Physics, Eds. B Galperin, PL Read, pp. 292-305. Cambridge: Cambridge Un. Press

Berloff, P., I. Kamenkovich, and J. Pedlosky, 2009: A mechanism of formation of multiple zonal jets in the oceans. J. Fluid Mech., 628, 395-425.

Brandt P, Hormann V, Bourles B, Fischer J, Schott FA, et al. 2008. Oxygen tongues and zonal currents in the equatorial Atlantic .J. Geophys. Res.-Oceans 113

Buzzicotti, M., B. A. Storer, H. Khatri, S. M. Griffies, H. Aluie 2023. Spatio-temporal coarse-graining decomposition of the global ocean geostrophic kinetic energy. J. Adv. Mod. Earth Sys., 15.

Carroll D, Menemenlis D, Dutkiewicz S, Lauderdale JM, Adkins JF, et al. 2022. Attribution of space-time variability in global-ocean dissolved inorganic carbon. Global Biogeochem Cycles 36: e2021GB007162

Chen R, Flierl GR, Wunsch C. 2015. Quantifying and interpreting striations in a subtropical gyre: a spectral perspective. J. Phys. Oc. 45: 387-406

Cornillon, P., and . others, 2019: Oceans. Zonal Jets. Phenomenology, Genesis and Physics, B. R. Galperin, P. L.Read , Ed., Camb. Un. Press, 46-71.

de Miranda, A. P., B. Barnier, and W. K. Dewar, 1999: On the dynamics of the Zapiola Anticyclone. J. Geophys. Res.-Oceans , 104, 21137-21149.

Ekman, V. W., 1905: On the influence of the earth's rotation on ocean-currents. Arkiv for Matematik, Astronomi och Fysik 2, 11, 52 pp.

Forget G. 2010. Mapping ocean observations in a dynamical framework: A 2004-06 ocean atlas. J. Phys. Oc. 40: 1201-21

Forget, G., J.-M. Campin, P. Heimbach, C. Hill, R. Ponte, and C. Wunsch, 2015: ECCO version 4: an integrated framework for non-linear inverse modeling and global ocean state estimation. Geosci. Model Dev., 8, 3071?3104.

Fukumori, I. Heimbach, P.Ponte, R. M.Wunsch, C. 2018: A dynamically-consistent ocean climatology and its temporal variations. Bulletin Amer. Met. Soc., October, 2107-2127.

Fukumori, I., O. Wang, I. Fenty, G. Forget, P. Heimbach, and R. M. Ponte, 2019: ECCO Version 4 Release 4, https://ecco.jpl.nasa.gov/drive/files/Version4/Release4/doc/v4r4_synopsis.pdf.

Galperin B, Read PL., Eds. 2019. Zonal Jets: Phenomenology, Genesis, and Physics.Cambridge Un. Press, Cambridge

Garabato ACN, Yu X, Callies J, Barkan R, Polzin KL, et al. 2022. Kinetic energy transfers between mesoscale and submesoscale motions in the open ocean?s upper layers. J. Phys. Oc. 52: 75-97

Gaspar, P., Y. Grėgoris, and J. M. Lefevre, 1990: A simple eddy kinetic energy model for simulations of the oceanic vertical mixing: Tests at station Papa and Long-term Upper Ocean Study site. J. Geophys. Res.-Oceans , 95, 16179-16193.

Gebbie, G. 2021: Combining modern and paleoceanographic perspectives on ocean heat uptake. Ann. Revs. Mar. Sci, 13, 16.1–16.27

Gent, P. R., and J. C. Mcwilliams, 1990: Isopycnal mixing in ocean circulation models. J. Phys. Oc., 20, 150-155.

Hogg, N. G. and W. B. Owens 1999: Direct measurement of the deep circulation within the Brazil Basin. Deep-Sea Res. Part II: Topical Studies in Oceanography, 46, 335-353

Huang RX. 2010. Ocean Circulation: Wind-driven and Thermohaline Processes. Cambridge ; New York: Cambridge University Press. xiii, 791 p. pp.

Leetmaa A, Niiler P, Stommel H. 1977. Does the Sverdrup relation account for the Mid-Atlantic circulation? J. Mar. Res., 35: 1-10

Liang, X., M. Spall, and C. Wunsch, 2017: Global ocean vertical velocity from a dynamically consistent ocean state estimate. J. Geophys. Res. , 122, 8208-8224.

McWilliams JC, Huckle E, Liang JH, Sullivan PP. 2012. The wavy Ekman layer: Langmuir circulations, breaking waves, and Reynolds stress. J. Phys. Oc. 42: 1793-816

Mazloff, M. R., P. Heimbach, and C. Wunsch, 2010: An eddy-permitting Southern Ocean state estimate. J. Phys. Oc., 40, 880-899.

McDougall, T. J., 1995: The influence of ocean mixing on the absolute velocity vector. J. Phys. Oc., 25, 705-725.

Menemenlis, D., and Coauthors, 2008: ECCO2: High resolution global ocean and sea ice data synthesis. Mercator Ocean Quarterly Newsletter, 31, 13-21.

Munk, W., L. Armi, K. Fischer, and F. Zachariasen, 2000: Spirals on the sea. Proc. Roy. Soc. A: 456, 1217-1280.

Nguyen, A. T., H. Pillar, V. Ocana, A. Bigdeli, T. A. Smith, and P. Heimbach, 2021: The Arctic subpolar gyre state estimate: Description and assessment of a data-constrained, dynamically consistent ocean-sea ice estimate for 2002-2017. J.of Adv. Modeling Earth Sys, 13, https://doi.org/10.1029/2020MS002398.

Olbers D, Willebrand J, Eden C. 2012. Ocean Dynamics. Berlin ; New York: Springer. 1 e (xxiii, 704 p.) pp.

Pedlosky, J., 1982: Geophysical Fluid Dynamics. Springer Verlag,, xii, 624 pp..

Pedlosky J. 1996. Ocean Circulation Theory. Berlin ; New York: Springer. xi, 453 pp.

Phillips, N. A., 1963: Geostrophic motion. Rev. Geophys., 1, 123-176.

Price, J. F., R. A. Weller, and R. Pinkel, 1986: Diurnal cycling: Observations and models of the upper ocean response to diurnal heating, cooling, and wind mixing. J. Geophys. Res.-Oceans , 91, 8411-8427.

Price, J. F., and R. A. Weller, Schudlich, R. R., 1987: Wind-Driven Ocean Currents and Ekman Transport. Science, 238, 1534-1538.

Redi, M. H., 1982: Oceanic isopycnal mixing by coordinate rotation. J. Phys. Oc. 12, 1154-1158.

Rogers, M., Ferrari, R., Nadeau, L.-P.2023: Mid-depth recipes J. Phys. Oc. 53,https://doi-org.libproxy.mit.edu/10.1175/JPO-D-22-0225.1.

Shrira, V. I., and R. B. Almelah, 2020: Upper-ocean Ekman current dynamics: a new perspective. Journal of Fluid Mechanics, 887.

Stommel, H., and F. Schott, 1977: The beta spiral and the determination of the absolute velocity field from hydrographic station data. Deep-Sea Res., 24, 325-329.

Talley LD, Pickard GL, Emery WJ. 2011. Descriptive Physical Oceanography : An Introduction. Amsterdam ; Boston: Academic Press. viii, 555 pp., [60] p. of plates.

Tamsitt, V., and Coauthors, 2017: Spiraling pathways of global deep waters to the surface of the Southern Ocean. Nature Communications, 8, 172.

Thomas MD, De Boer AM, Johnson HL, Stevens DP. 2014. Spatial and Temporal Scales of Sverdrup Balance. J. Phys. Oc. 44: 2644-60

Vallis, G. K., 2017: Atmospheric and Oceanic Fluid Dynamics: Fundamentals and Large-Scale Circulation. 2nd ed. Cambridge Un. Press, 946 pp.

Wang Q, Dong C, Dong J, Zhang H, Yang J. 2022. Submesoscale processes-induced vertical heat transport modulated by oceanic mesoscale eddies. Deep-Sea Res. Part II: Topical Studies in Oceanography 202: 105138

Wilson, E. A., A. F. Thompson, A. L. Stewart, and S. Sun, 2022: Bathymetric control of subpolar gyres and the overturning circulation in the Southern Ocean. J. Phys. Oc., 52, 205-223.

Wolfe, C. L., and P. Cessi, 2010: What sets the strength of the middepth stratification and overturning circulation in eddying ocean models? J. Phys. Oc., 40, 1520-1538.

Wunsch, C., 2023: A simplified ocean physics? Revisiting abyssal recipes. J. Phys. Oc., *J. Phys. Oc., 55,*1387–1400, 2023.

Wunsch, C. and R. Ferrari, 2018: 100 Years of the ocean general circulation. Meteorological Monographs, 59, pp.7-1.

Wunsch, C., and P. Heimbach, 2007: Practical global oceanic state estimation. Physica D-Nonlinear Phenomena, 230, 197-208.